SIMULATION AND EXPERIMENTATION OF DROPLETS ON MICRO-PATTERNED SURFACES

BY

BANGLIN LIU

THESIS

Submitted in partial fulfillment of the requirements
for the degree of Master of Science in Mechanical Engineering
in the Graduate College of the
University of Illinois at Urbana-Champaign, 2014

Urbana, Illinois

Advisers:

Professor K. Jimmy Hsia
Associate Professor Sascha Hilgenfeldt

ABSTRACT

We developed a robust simulation tool that provided energetic and geometric information of droplets deposited on patterned surfaces. Deformation of the droplet in response to discrete features in the contact plane was examined and quantified on an energy basis. Additionally, quasi-static simulation of relative movement between droplet and substrate was performed. Energy-displacement response of the droplet was found to exhibit surface tension-dominated elastic behavior.

Experimental effort was carried out in combination with simulations. Using a novel technique, synchronized video and force response were obtained for droplets moving on patterned PDMS substrate. Features present in the force-displacement data were analyzed and linked to various aspects of the droplet-substrate system, including surface modes of the pinned droplet, residual liquids deposited behind the trailing edge, and geometric parameters of the substrate pattern.

TABLE OF CONTENTS

LIST OF SYMBOLS

θ	Contact Angle
ρ_g	Density, Gas
ρ_l	Density, Liquid
R	Droplet Radius
V	Droplet Volume
g	Gravity
γ_{lg}	Surface Tension, Liquid-Gas Interface
γ_{ls}	Surface Tension, Liquid-Solid Interface
γ_{sg}	Surface Tension, Solid-Gas Interface
μ	Viscosity, Dynamic
ν	Viscosity, Kinematic

LIST OF FIGURES

LIST OF TABLES

Introduction

Micro-patterned super-hydrophobic surfaces have sparked a wide range of research interest due to potential applications including self-cleaning[1-2] and particle deposition[3-5]. The key focus of the research effort lies in understanding the interaction between liquid droplet and patterned surfaces. The classical Cassie-Baxter model attributes averaged homogeneous properties to the surface[6] and is generally considered sufficient when the scale of the surface features is much smaller than the deposited droplet. The Cassie-Baxter model however does not address contact angle hysteresis (CAH), a commonly observed phenomenon where movement of the droplet alters local contact angle within a maximum and minimum value known as the advancing and receding contact angles. Traditional approaches in understanding CAH include gravity-driven droplet on tilted surface[7-9] and evaporation/volume injection[10-11], and are generally limited to contact angle measurement and image capture. A novel method was recently proposed which enabled synchronized image capturing and resistant force measurement[12]. Figure 0.1 shows a schematic of the experimental setup. First a micro-patterned PDMS substrate is placed on a microscope stage. A droplet is then deposited on the substrate and held in position via contact with a stationary force probe. As the microscope stage is driven away by a step motor, the probe registers resistance force between the droplet and the substrate, and a high speed camera connected to the microscope provides simultaneous graphic information.

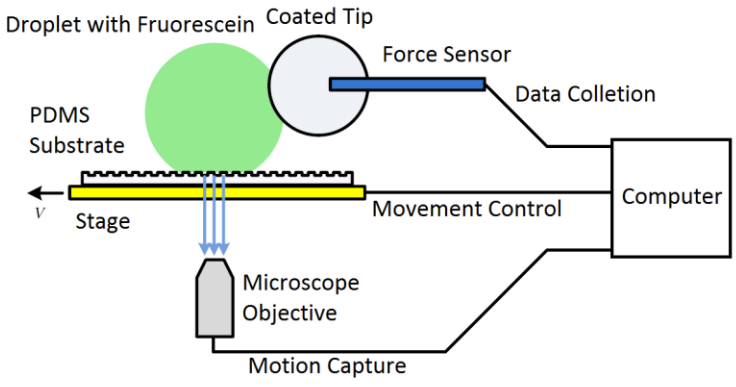

Figure 0.1: Schematic of experimental setup

As a continuation of the effort, we performed computational and experimental analysis of droplets on patterned PDMS substrates. Various aspects of droplet-substrate interaction were studied via a combination of Surface Evolver[13] simulation and frequency analysis; correlations between the force-displacement data and geometric features of the substrate were established.

1. Computational Approach

The goal of this section was to develop a simulation tool capable of assessing the energy change of a liquid droplet placed on patterned surfaces upon deformation and displacement. In particular we were interested in the effects of pinning and depinning from individual pillars on the geometry and energy of the bulk droplet. Thus a complete model of the substrate and the droplet with high resolution was needed. In addition, the tool should also be able to handle variables including surface properties, pattern geometry and orientation, and gravity/ inclination.

1.1 The Surface Evolver

The software package Surface Evolver (SE) was chosen to handle the simulation aspect of the study. Developed and maintained by Kenneth Brakke, SE is a finite element program that minimizes surface energy functionals of custom geometries[13]. Specifically, the input surface is refined and evolved toward a local minimal energy state via steepest descent/conjugate gradient method. SE supports custom geometric constraints as well as energy functions and is therefore particularly useful in simulating surface energy-dominated scenarios coupled with complex geometries. Indeed, successful SE applications had already been demonstrated in a number of studies including liquid droplet geometry on grooved patterns[14], mechanical response of solder joint[15-16], and contact angle measurement of droplet on square pillars[17].

1.2 Modeling Considerations

By design of SE, bodies are represented as the enclosure of triangular facets oriented by the surface normal. Thus a droplet in Cassie-Baxter mode would only require modeling of the wetted top surfaces of the pillars plus the free liquid-gas interface. To this end, we used the difference between surface energies of the liquid-solid interface, γ_{ls}, and that of the solid-gas interface, γ_{sg}, to define the pillar facets of the droplet, and used the liquid-solid interface energy, γ_{lg}, to define the free facets. The surface energy difference $\gamma_{ls} - \gamma_{sg}$ was chosen for the pillar facets to represent the energy change incurred by contact line movement. In addition, using the energy difference also eliminated the need

to track dewetted pillar facets and thus sped up the simulation. Figure 1.1 shows a schematic of the surface energy assignment.

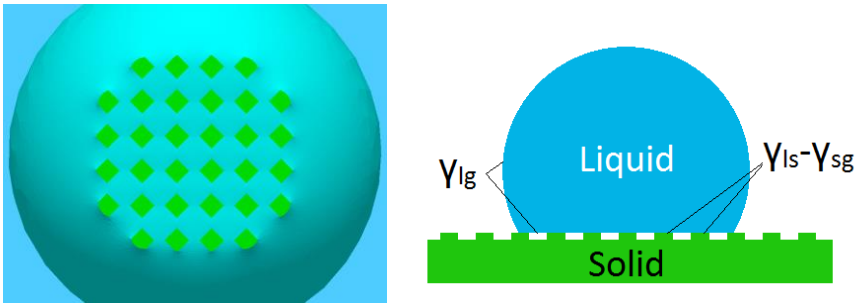

Figure 1.1: (right) definition of interface energies; (left) screen shot of actual model run in SE. Note that the solid-gas interface was never modeled due to the usage of the interfacial energy difference $\gamma_{ls} - \gamma_{sg}$.

Boundaries of the liquid-solid interface were defined via one-sided geometric constraints in anticipation of partially wet pillars. In particular, facets on the liquid-solid interface (green patches in Figure 1.1) were forbidden to extend beyond their perspective pillar boundaries but were otherwise free to translate and deform in the 2D plane.

Concerning the contact angle constraint, two different approaches were used. The first one was a straight forward implementation of Young's equation:

$$0 = \gamma_{sg} - \gamma_{ls} - \gamma_{lg} cos\theta \tag{1.1}$$

Figure 1.2 shows a schematic of surface tension balance at the three phase contact line.

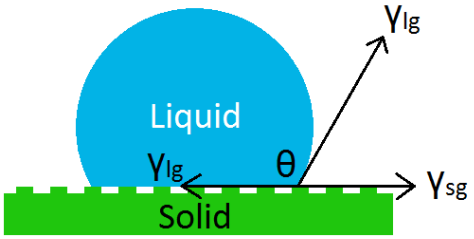

Figure 1.2: schematic for Young's Equation

Once the surface energies were defined, an area integration was performed. Area of each facet was first modified by the local surface energy and then added to the global energy.

As discussed by Brakke, however, convergence tends to be slow using this method due to the fact that local geometric change did not immediately affect elements further away.

The second method involved a line integral performed around the boundary of each pillar facet in the contact region. By Green's theorem:

$$\oint_C (\mathrm{Ldx} + \mathrm{Mdy}) = \iint_D \left(\frac{\partial \mathrm{M}}{\partial \mathrm{x}} - \frac{\partial \mathrm{L}}{\partial \mathrm{y}}\right) \mathrm{dxdy} \tag{1.2}$$

Here D is the region bounded by the piecewise smooth, oriented curve C. Choosing $M = x$ and $L = 0$ gives the enclosed area:

$$\mathrm{A} = \oint_C \mathrm{xdy} \tag{1.3}$$

Thus the wet area on each pillar could be extracted from the boundary edges only, omitting usage of the elements further inside and speeding up the calculation. However, this method relied heavily on the orientation of the boundary edges. Coupled with the usage of one-sided constraints, the line integral method was found to have led to extremely distorted and unrealistic geometries in some cases.

In practice, choice of the implementation method depended on the scenario involved. Whereas the line integral was generally faster, some cases specifically required using the area integral. For example, the attachment event resulting from contact line advancement involved a small contact area that underwent rapid expansion, which could only be stably simulated using an area integral. More information will be provided in section 1.4.1.

Another key aspect of modeling the droplet was to design an efficient refining scheme. A high level of refinement was desired near the substrate for better accuracy in simulating effects from the additional discrete structures. However, it would be unrealistic to extend the level of resolution to the rest of the model, as the droplet could potentially cover tens or hundreds of pillars. Therefore we used an adaptive meshing scheme that focused on features closest to the contact line. For example, wetted pillar facets that are close to the origin were never refined; facets on the free liquid-gas interface that were high above the substrate were never refined either. The program handled the refining by mapping geometric features (vertices, edges and facets) to the grid of pillars and checking for

proximity to any boundary pillars. Figure 1.3 shows the contact plane of a typical model with higher mesh resolution near the boundary. In practice, features that were not refined still participated in the evolution of the model, so in longer simulations the selective meshing scheme could be less effective due to vertex averaging.

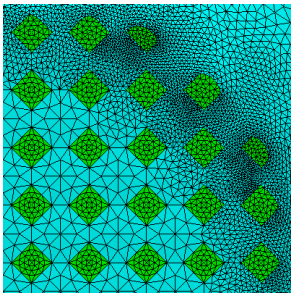

Figure 1.3: bottom view of the contact plane showing higher level of refinements near boundary pillars.

1.3 Implementation

Framework of the codes was established by Mike Grigola[18] and was adapted for the need of this study. SE reads in geometric and energy information of the model through text files of a required format (.fe). The process was typically done by manual input of a simple model which was then refined in the program, but for the model scale and complexity involved in this study (20-500 vertices before refinement with 30-100 pillars each having its own set of constraints) such a task became highly inefficient. Additionally, manual input could not provide enough coverage on the parameters of interest, which included droplet volume, pillar shape and size, fraction of pillar top area to total projected area of the substrate, etc. Therefore a Mathematica routine was written to handle the text output. Figure 1.4 shows a series of screen shots in a typical modeling process. The program first estimated the contact area using the droplet volume and contact angle. The grid of the substrate was then laid out based on the dimensions of the contact area. Each grid point represented a pillar and the geometric information of the pillar top was then filled in. Unless the pillars had extreme shapes, tessellation of the liquid-gas interface between pillars was done by deformed octagons. The final step added a dome representing the droplet, which was automatically refined in SE based on surface energy and volume constraints. Depending on the nature of the simulation, symmetry might be used in the routine.

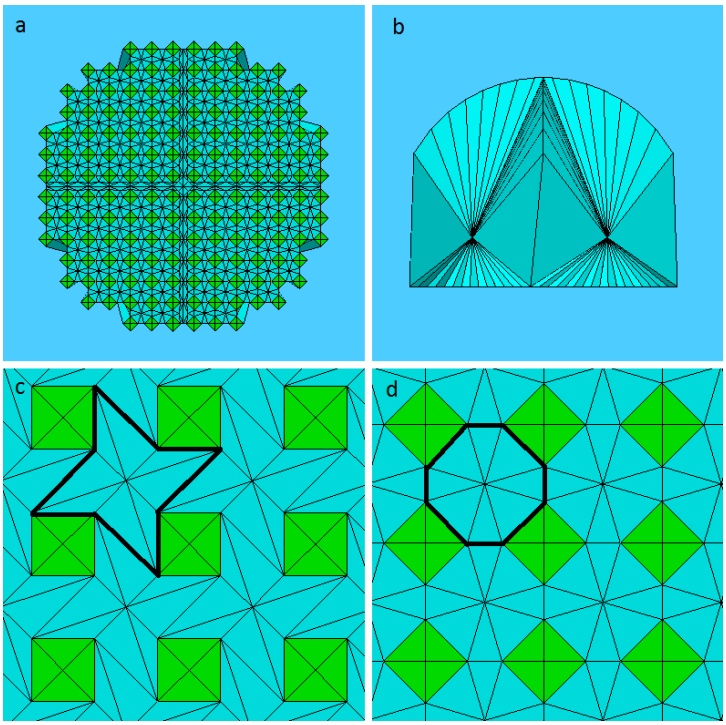

Figure 1.4: (a) contact plane of an axisymmetric model showing the pillar grid. Green patches represent pillars. Note the x- and y- symmetry axes; (b) front view of the dome structure added to complete the model; (c,d) octagons used for the tessellation of the contact plane between pillars in rectangular (c) and staggered (d) arrangements.

To accommodate the variety of substrate patterns used in the experiments, the program was designed to support different pillar geometry as well as arrangements. Figure 1.5 shows a number of different configurations generated by the program.

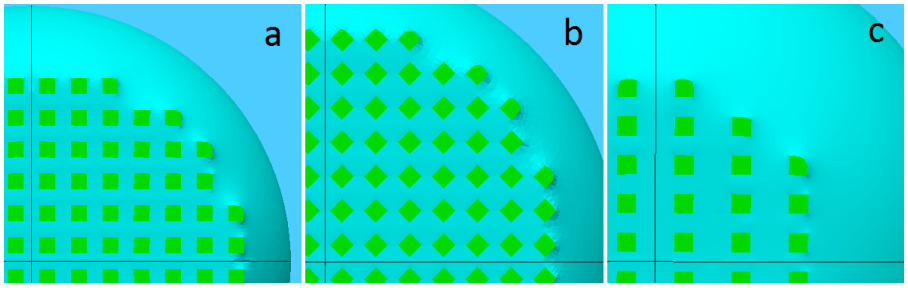

Figure 1.5: (a) square arrangement with 0.36 area coverage (pillar-to-substrate ratio, denoted α henceforth); (b) staggered arrangement with α=0.25; (c) 2:3 rectangular arrangement with α=0.17.

One of the key objectives of the simulation was to assess the effects of droplet movement on energy and local geometry. Since contact with the substrate was enforced by

geometric constraints which could not be added or removed automatically by SE, it was imperative to develop a procedure that checks for potential attachment and detachment sites on the substrate and enacts the corresponding processes. Grigola proposed an empirical method[18] which checked for boundary vertices that were too far from their starting position and used them as criteria for detachment (droplet depinning) (see Figure 1.6).

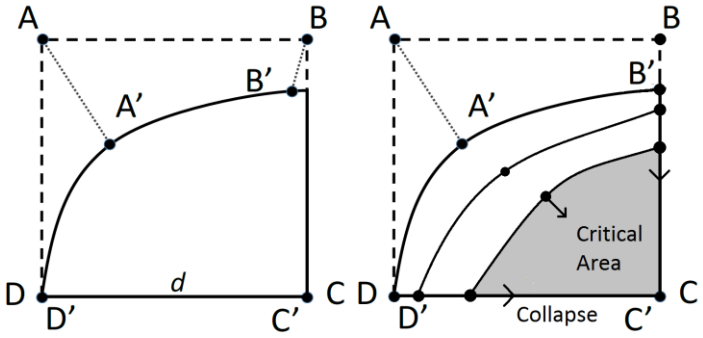

Figure 1.6: schematic showing the depinning criteria. The curve D'-A'-B' represents the contact line on a square pillar ABCD. (Left) Depinning by critical distance: if any of the segments AA', BB' and DD' exceeds a prescribed critical length, the polygon A'-B'-C'-D' will be removed from the contact plane. (Right) Depinning by area coverage: The contact line D'-A'-B' is forced to recede by reducing droplet volume stepwise. Below a critical volume, contact with the pillar becomes unstable and the curve D'-A'-B' collapses toward C. The area coverage right before the collapse is used as the detachment criteria.

A slightly different version of the method based on area coverage was used in the actual code. A critical ratio was used to check if enough fraction of the top of a pillar was dewetted. Once the criterion was met, all remaining facets on the particular pillar top would be detached. To determine the proper critical coverage, we constructed a simulation where the volume of a static droplet was reduced in discrete steps. Each reduction would result in a discrete displacement of the contact line, and it was observed that there existed a critical area coverage below which attachment to the pillar was no longer stable. Figure 1.6 shows a sketch of the simulation. The unstable area coverage was then used as the detachment criterion.

Implementation of attachment event was designed in a similar manner. First, all facets directly above an unattached pillar were checked for their distances to the pillar top. If the closest facet was within an empirically determined critical distance, all its vertices would

be attached to the surface. To determine the critical distance, we selected facets at different distances from the substrate and forced them to attach to the pillar below. Then simulations were run to determine if the attachment was stable (the attached facet expanded or retained a constant area) or unstable (the attached facet contracted toward a single vertex and halted the simulation). The maximum distance above which attached facets became unstable was then used as the attachment criterion. Figure 1.7 shows a sketch of the above simulation.

Figure 1.7: schematic showing the pinning criterion. (a) Configuration before pinning. (b) The facet closest to an unattached pillar is pinned. (c) The pinning is stable if the pinned facet does not collapse when evolved. (d) If the pinned facet destabilizes (in this case collapses into a corner), then the attached pillar fails the criterion. The critical pinning distance is determined as the maximum facet-pillar distance beyond which a pinned facet never stabilizes.

As an energy minimizer, SE does not support dynamic simulations. However, the range of velocities over which experimental data was collected allowed for a quasi-static SE modeling of the motion. The capillary number is defined as

$$\mathrm{Ca} = \frac{\mu v}{\gamma_{lg}} \tag{1.4}$$

Here v is the velocity of the substrate. For the range of speed used in experiments (8-540μm/s) and testing liquid (water/1:1 water-glycerol), Ca ranged from $1.11\text{x}10^{-7}$ to 0.0119 and viscous force could be safely neglected. To implement the droplet-probe contact, a separate constraint was applied to a facet on the leading side of the droplet. The constraint forced the facet to conform to the surface of a sphere centered away from the droplet with a prescribed radius matching that of the actual probe tip. The constrained facet was then refined and the droplet evolved until the entire droplet attained a stable geometry. Figure 1.8 shows a comparison between a constrained droplet model and a photo of the actual experimental setup. Motion of the substrate was then implemented by

moving the center of the spherical constraint away in discrete steps, and the droplet was allowed to converge after each displacement.

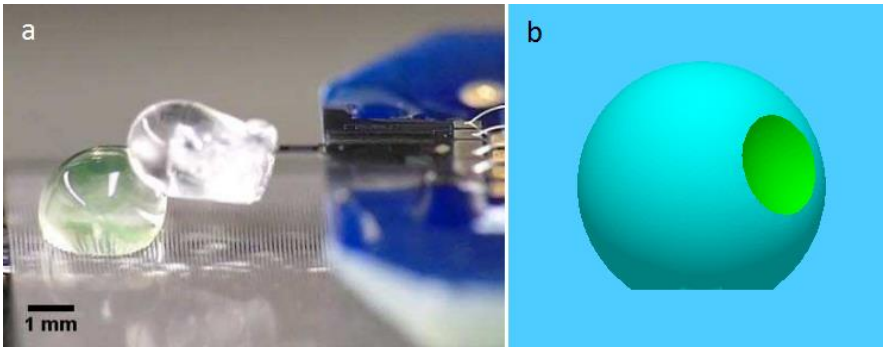

Figure 1.8: (a)[12] droplet attached to a PDMS blob glued to the force sensor; (b) model of the constrained droplet.

1.4 Results and Discussion

1.4.1 Static Droplet

We first attempted to quantify the deformation and the associated energy change due to the addition of discrete features to a homogeneous substrate. A droplet with fixed volume was placed on an array of square pillars and allowed to refine and converge. To measure the deviation from a cylindrically symmetric droplet (which would be the case on a smooth surface), a small patch with constant azimuthal and polar span ($\Delta\phi$ and $\Delta\theta$ respectively) was defined. Figure 1.9 shows a schematic of the patch definition. Total surface energy of the patch was measured and recorded as the patch was rotated around the polar axis.

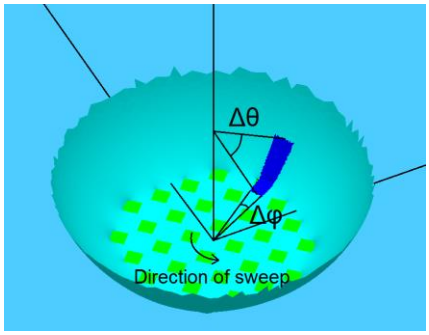

Figure 1.9: schematic of the sweeping patch definition.

Figure 1.10 shows the angular dependence of patch energy for three different polar spans ($\Delta\theta$ = 16^o, 30^o, and 48^o respectively). Overlays of the three plots each with their mean value set to zero could be found in Figure 1.11. The higher noise level of the $\Delta\theta$ = 30^o curve could be explained by the increased number of facets included in the patch. Nevertheless, the energy variation along the two curves was highly consistent. This finding provided strong evidence that the deformation and energy change due to the patterned features only affected facets in close proximity to the substrate, while the upper structure of the droplet remained azimuthally symmetrical. We believed that this localized nature of the energy fluctuation could potentially lead to a less complex 2D model of the system with reasonable accuracy.

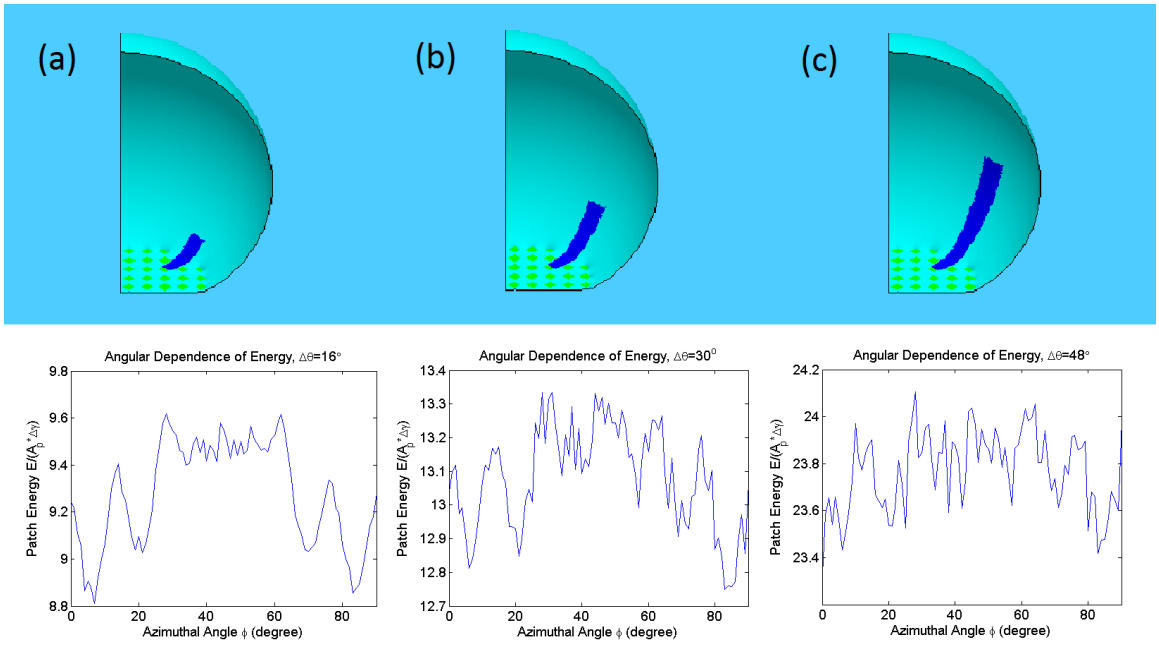

Figure 1.10: patch energy vs. angle plots for three meridional spans. (a) Δθ=16^0; (b) Δθ=30^0; (c)Δθ=48^0. Energy was scaled using the surface energy of one full wetted pillar, $A_p * \Delta\gamma$, where A_p is the pillar top area, and $\Delta\gamma = \gamma_{ls} - \gamma_{sg}$. This scale represents the energy change due to the dewetting of one pillar. The three patches end at the same polar angle θ=63^0 while the starting angle varies depending on the polar span.

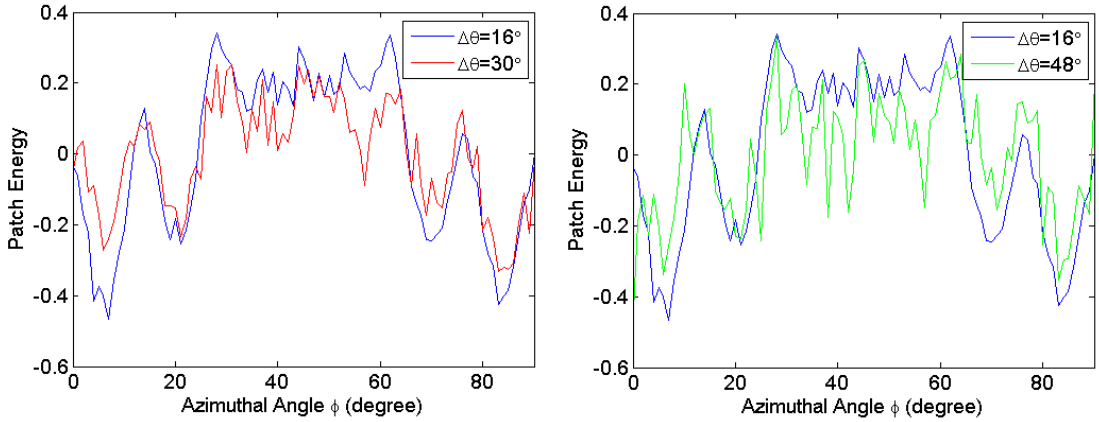

Figure 1.11: overlay plots of (left) $\Delta\theta=16^0$ and $\Delta\theta=30^0$; (right) $\Delta\theta=16^0$ and $\Delta\theta=48^0$. Since the simulation used an adaptive meshing scheme (see Figure 1.3), patches with greater meridional spans included facets higher above the contact plane that were usually less refined. Effects of the discretization were manifested in the higher level of noise for larger patches. Nevertheless, the overall trends of energy variation are clearly consistent at different patch sizes.

Figure 1.12a shows the energy plot of the $\Delta\theta=16^0$ patch with pillar locations marked. A closer examination of the energy plot revealed some interesting features of the droplet. First of all, orientation of the contact line segments had a strong influence on the local surface energy. The short plateau between the third and fifth pillars ($29\text{-}61^0$) corresponded to the 45-degree segment of the contact line, whereas along the vertical and horizontal directions (0 to 29 and 61 to 90 degrees respectively) the patch energy was found to be lower. In addition, when the patch resided right above a boundary pillar (pillars 1, 2, 6 and 7), the plot showed a decrease in the total surface energy of the patch. Given the lower surface tension of the solid-liquid interface (0.036N/m), the drop in the energy plot could either be due to reduction of patch area or due to a locally lower energy density. To isolate the geometric effects, a separate plot showing only the area variation was made (Figure 1.12b). The plot was obtained by setting all facets on the droplet to liquid-gas interface while using the converged geometric shape from the previous measurement. If we define the nominal orientation of the contact line to be the directions of line segments connecting neighboring boundary pillars, then the peaks at 29 and 61 degrees corresponded to locations where nominal orientation of the contact line changed from vertical to 45 degree, and 45 degree to horizontal respectively (pillars 3 and 5).

Additionally, the central pillar (#4) also imposed an area penalty as a pinning site along a contact line segment. In contrast, reductions of patch energy observed at pillar 1, 2, 6 and 7 proved to be result of density variation, since no distinct area change could be seen at the above sites in plot (b). Interestingly, the above mentioned polygonal appearance of the contact line was also observed in experiments of static droplets. Figure 1.13 shows photos taken at the contact plane of stationary droplets, where the contact line also adopted octagonal shapes. Based on the above findings, we postulate that the polygonailty observed in the contact shapes of droplet is a compromise between minimizing the number of pinning sites along the contact line (each of which impose an area penalty from local deformation) (i.e. more circular), and minimizing the total number of turns in the nominal direction of contact line segments that also incur additional area for the structure (i.e. more square-like).

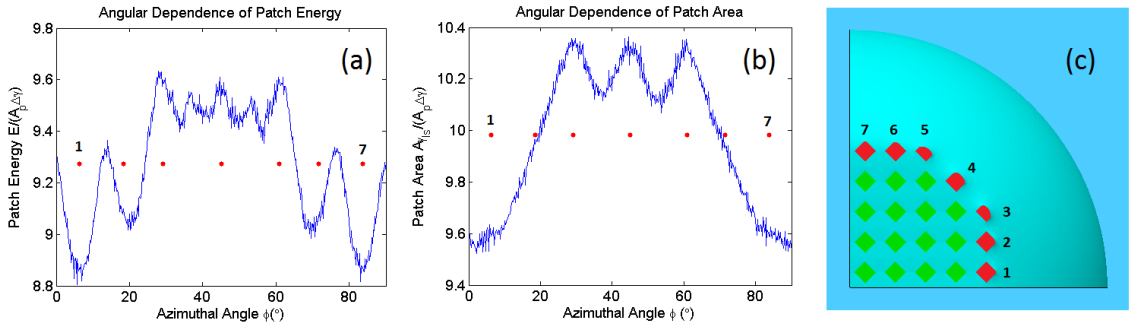

Figure 1.12: (a) Total patch energy as a function of azimuthal angle. The same energy scale $A_p(\gamma_{ls} - \gamma_{sg})$ is used (Figure 1.10). (b) Total patch area as a function of azimuthal angle. The non-dimensional area took the form $A^* = \frac{A\gamma_{lg}}{A_P(\gamma_{ls}-\gamma_{sg})}$. Red dots mark the location of boundary pillars, illustrated in (c).

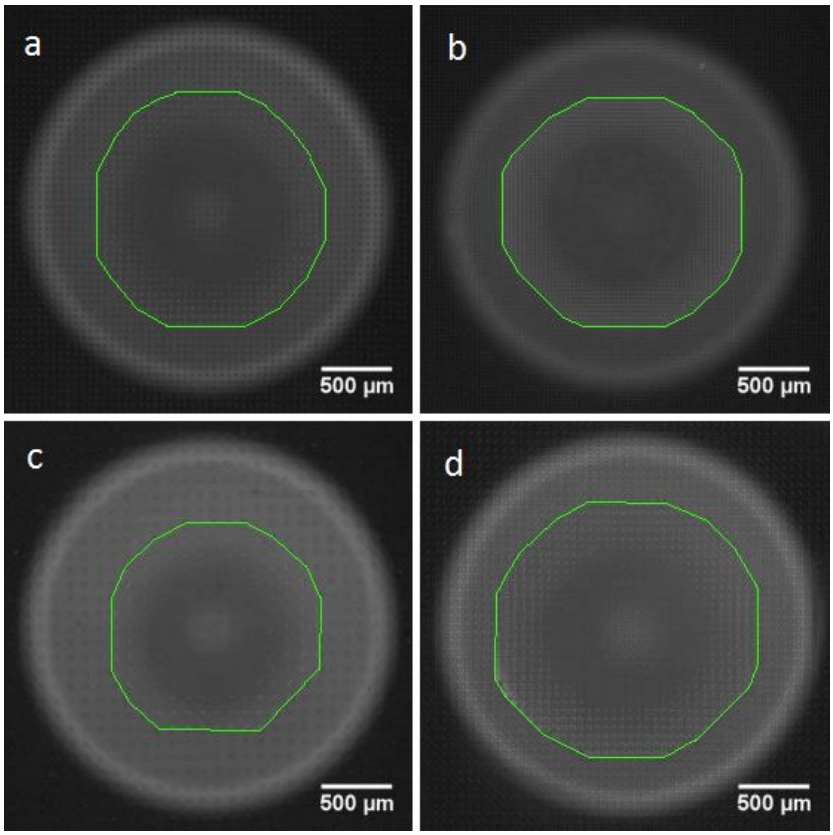

Figure 1.13[12]: photos of contact plane. Contact lines are highlighted in green. A 10uL droplet was deposited on four substrates of circular pillars with diameter D and area fraction α. From a) to d): D=27.3um, α =0.20; D=26.7um, α =0.59; D=43.7um, α =0.13; D=43.7um, α =0.38. The higher area fraction samples, b) and d), display stronger polygonal character in their contact area perimeters.

1.4.2 Droplet in Motion

As was discussed in section 1.3, the range of droplet velocities used in the experiments allowed for a quasi-static assumption for droplet shapes during motion. It was therefore possible to reproduce the dynamic energy response of the droplet on a frame-by-frame basis. Specifically, a geometric constraint was applied to a section of the leading liquid-gas interface. The constraint forced features on the interface to conform to a spherical surface to mimic the presence of the polymer coating on the force probe during dynamic experiments. Motion was implemented by displacing the center of the spherical constraint in discrete steps, and the droplet was allowed to reach stable geometry at each step, upon which energy and overall geometry of were recorded. Figure 1.14 shows a series of screen shots of the contact plane over a full period of motion (detachment of a full

column of pillars). An energy vs. displacement plot of the process is plotted in Figure 1.15. The energy-displacement curve was very well fit by a quadratic function, with an effective spring constant of 0.0726N/m. Since the liquid-gas interface was defined with a surface energy of 0.073 N/m, we believed the above spring constant was a result of the elastic nature of the droplet model.

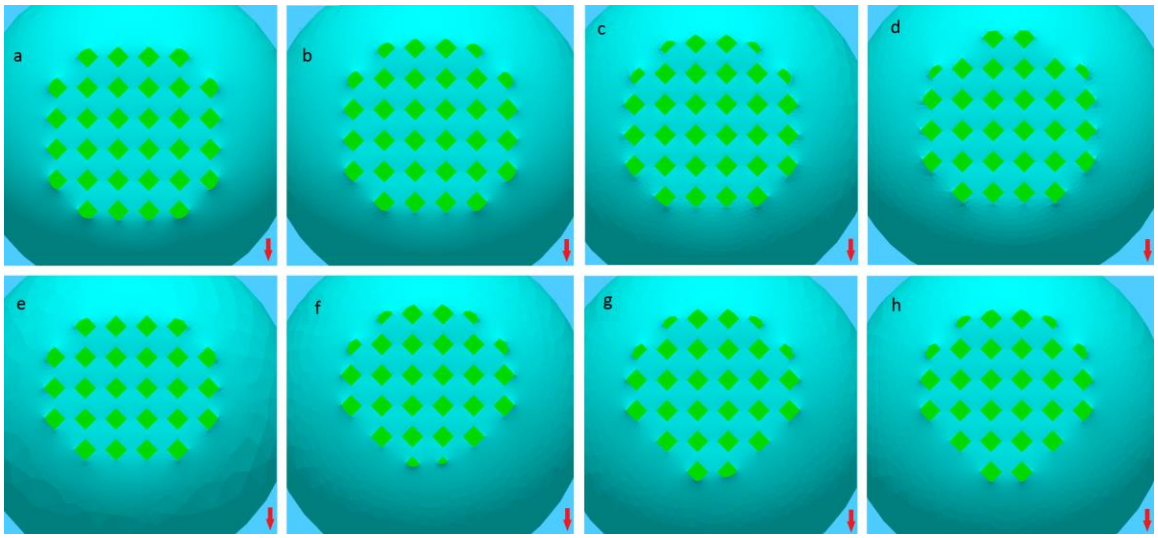

Figure 1.14: Contact surface morphology during pillar detachment and attachment. The droplet is displaced against the substrate by varying the center of the spherical constraint stepwise (a-h). Red arrow indicates the direction of displacement.

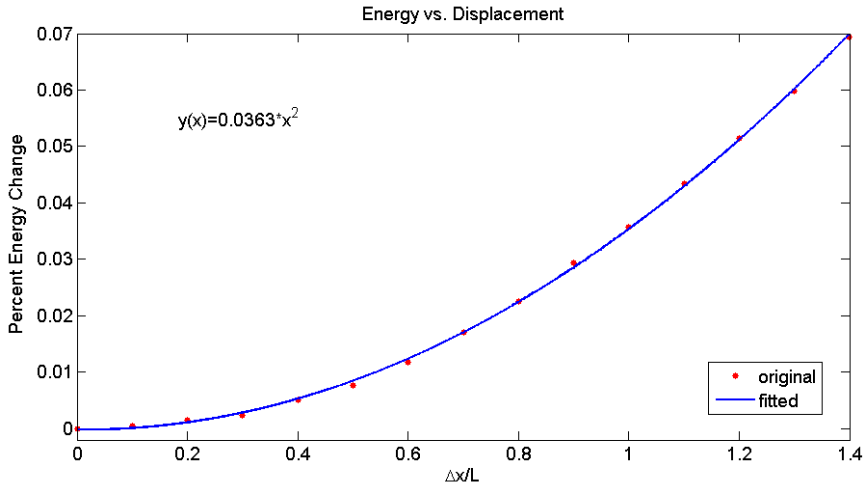

Figure 1.15: energy vs. displacement plot for droplet motion modeled in 1.14. A second order least square fit was performed to extract the effective spring constant. Displacement x was scaled by pillar spacing. Energy was scaled using the starting configuration (x=0). The actual fitting function included a first order and a constant term: $y(x)=0.03634x^2-7.893*10^{-4}x-1.996*10^{-4}$.

1.5 Conclusion

A robust simulation tool was developed that allowed for the study of various geometric parameters in droplet-on-patterned-surface scenarios. The static droplet deformed in response to substrate features and the deformation was found to be concentrated in close proximity to the substrate. On a square array of pillars the deformed droplet took on an octagonal contact area to minimize the net deformation penalty from discretization of the contact line. Dynamics of a droplet moving on a substrate was studied under a quasi-static assumption. The energy-displacement response exhibited second-order elastic behavior dominated by surface tension.

2. Experimental Work

A common way to investigate contact angle hysteresis involves usage of an inclined plane[7-9] (Figure 2.1). A sample is placed on a platform capable of rotating around a fixed axis. A droplet is then deposited on the sample and the platform is slowly tilted until gravity triggers motion of the droplet. In some more recent work[12] a novel method of dynamic force measurement was proposed. Rather than using an inclined plane to induce droplet movement, a capacitor force probe was used to horizontally drag a droplet along a patterned substrate while real time force data was recorded (see Figure 2.2a). In practice, a second microscope stage was used to position the force sensor prior to substrate movement. Figure 2.2b shows a photo of the supporting structure. Adhesion between the probe and droplet was provided by a small polymer sphere (diameter 800-1200 μm) attached to the probe tip (Figure 2.3a). Coupled with high-speed camera recordings, this method provided an opportunity to quantify the effects of droplet deformation on the overall force and energy response. A typical force-time measurement is shown in Figure 2.3b. A more detailed interpretation of the plot can be found in section 2.2.4. As a continuation of this effort, we conducted further experiments using the same technique.

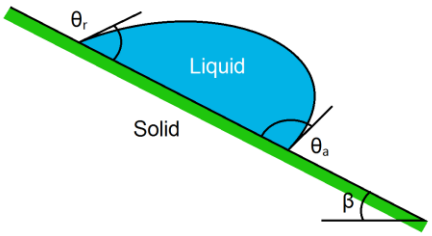

Figure 2.1: schematic of an inclined plane experiment. θ_a and θ_r are the advancing and receding contact angles respectively. β is the angle of inclination.

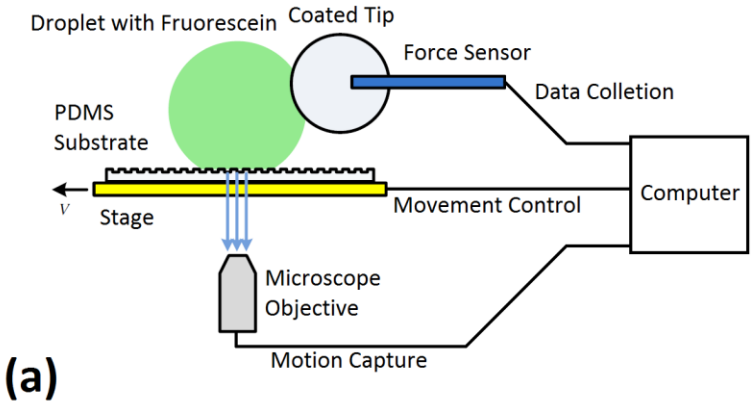

(a)

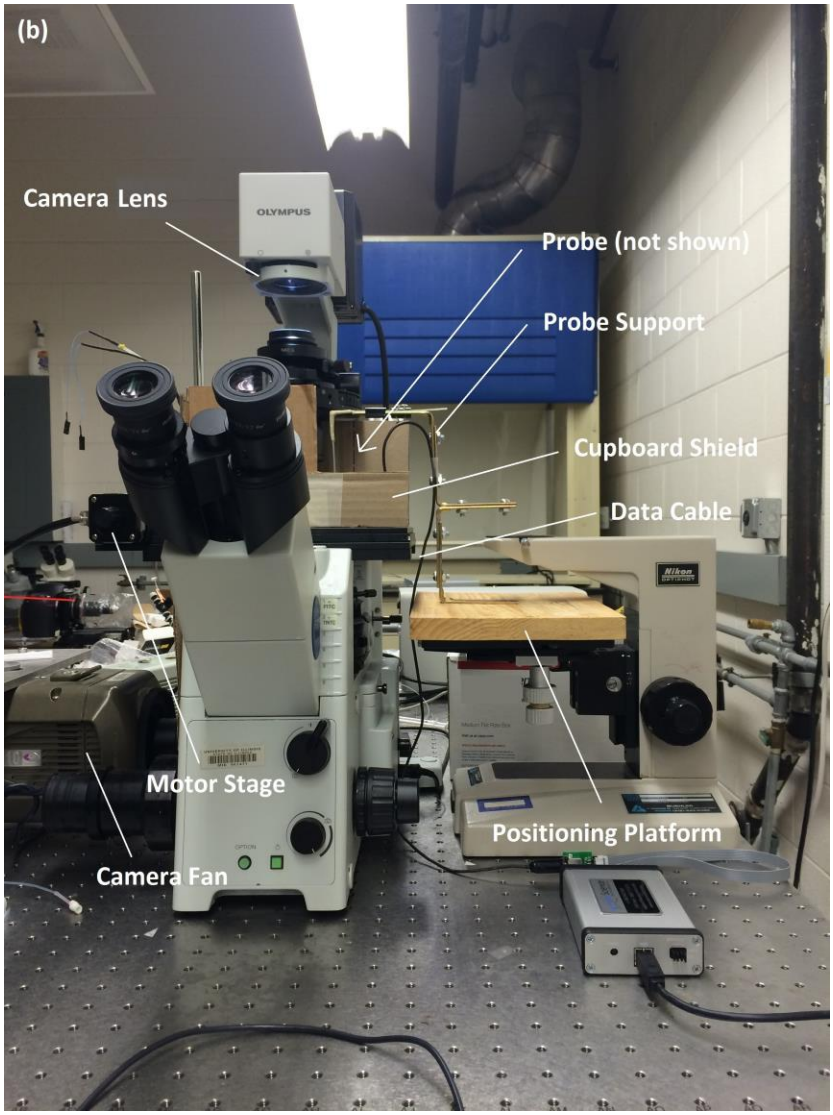

Figure 2.2: (a) (also Figure 0.1) schematic of the experimental setup in [12]. (b) Photo of the apparatus, including a second microscope platform (right) for positioning.

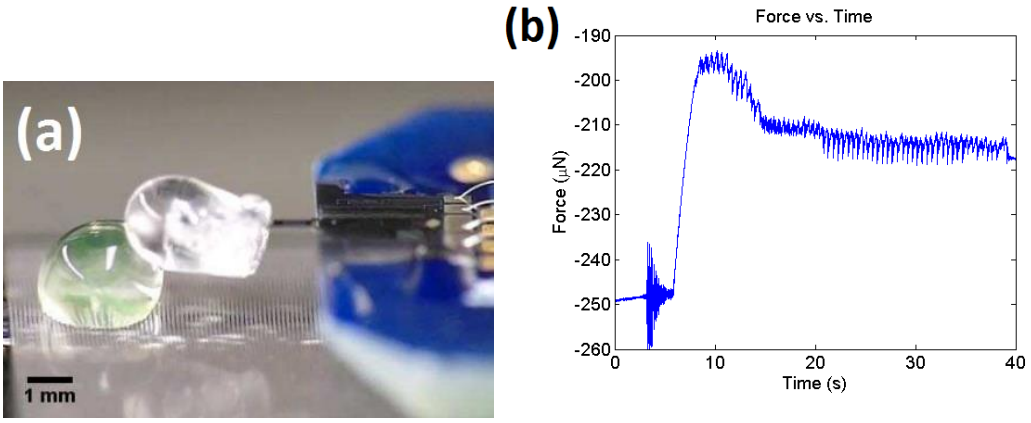

Figure 2.3: (a) (also Figure 1.8a) photo showing the attached PDMS sphere to the force probe in contact with a droplet. (b) A typical measurement of force-time series. Sample 3 (see Table 2.1) was used. Section 2.2.4 contains a detailed analysis of the plot.

2.1 Experimental Setup

2.1.1 Equipment

The experimental setup consists of three separate modules: motion control, image capture and data collection (see Figure 2.2). All equipment was placed on a hydraulic optical table for vibration damping. A PDMS sample was first placed on the stage of an inverted microscope (Olympus IX71). A droplet was then placed on the sample, and through movement of a separate three-axis stage a micro capacitor force probe was placed in contact with the droplet. Movement of the droplet was achieved by driving the microscope stage via a step motor while keeping the force probe stationary. Finally, image capture was done by a high speed camera (Phantom V310, Vision Research) connected to the microscope.

Two types of liquids were used in the experiments: DI water (1.00g/cm^3, 8.9x10^{-4}Pa·s) and a water-glycerol mixture with 1:1 volume ratio (1.13g/cm^3, 0.79Pa·s). To resolve the contact line between the droplet and the PDMS sample, fluorescein disodium ($C_{20}H_{10}Na_2O_5$, molecular weight 376.27g/mol) was added to the test liquids. For DI-water, fluorescein concentration was set at 10^{-4}mol/L (38 ppm). The water-glycerol mixture was prepared by mixing the dyed water with an equal volume of 97% glycerol, with resulting concentration of 5x10^{-5}mol/L (33 ppm). A mercury lamp with a 460nm

excitation filter was connected to the microscope. Emitted light (521nm) by the fluorescent dye was then detected by the objective under the PDMS sample.

The experimental setup offers a number of tunable parameters. Substrate speed and movement direction are controlled by a LabView module accompanying the motor stage. Video frame rate and exposure time can be adjusted in a separate camera control program. Additionally, the sampling rate of the force data can also be adjusted but is typically set to match the video frame rate.

2.1.2 Probe Treatment

The force probe used in the experiments (FT-S1000) employs a small silicon cantilever extending from a comb-drive (see Figure 2.4a) as the probe tip. The typical droplet volume in the experiments ranged from 2μL to 10μL. Given the size of the cantilever (50 μm x 100 μm x 3000 μm), additional treatment was required to generate enough adhesion between the probe and the droplet to prevent detachment of the probe. This was initially done by gluing a hollow PDMS sphere to the probe tip. Figure 2.3 shows a photo of a working probe with a PDMS sphere attached. The sphere was manufactured by applying layers of PDMS onto a gauge 23 syringe needle (0.64 mm outer diameter). To attach the sphere, the central opening was first filled with liquid superglue and then placed in contact with the probe tip until the glue cured. PDMS was chosen due to the relative simplicity of manufacturing desired shapes. Additionally, the hydrophobicity of the PDMS surface could keep deformation of the liquid droplet in contact to a minimum. However, since any direct contact between the sphere and the probe tip during the gluing process could potentially break the cantilever through bending, the attached sphere was limited to relatively large sizes (~ 2 mm in diameter) to accommodate for a large opening at the center. The procedure also caused problems when handling the treated probe, since the additional weight made bending failure much more likely.

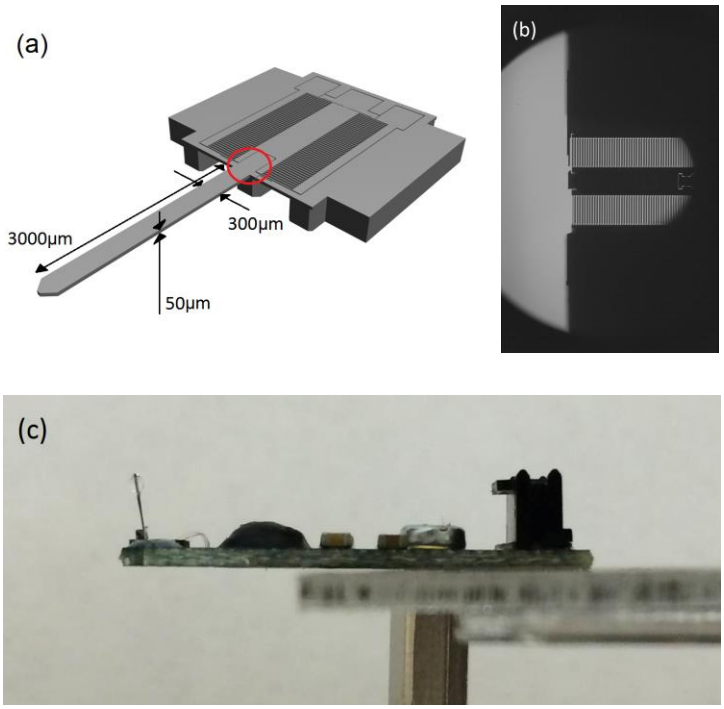

Figure 2.4: (a) schematic of the probe tip with dimensions, including a cantilever and a comb-drive (FT-S1000, FemtoTools). The red circle marks the location of the failure site; (b) microscope image of a failed probe tip. (c) photo of a failed dip-coated probe. The bending failure occurred during handling of the probe. The same failure mode was considerably more common among the glued probes (shown in Figure 2.3a) that had much heavier attachments. The broken tip was kept in contact with the chip by a thin PDMS layer that spread from the tip to the comb-drive. In other words, this probe was already damaged before the failure occurred.

Attempts were also made to directly dip coat the probe tip in liquid PDMS. The coating was then cured at room temperature to prevent heat damage to the probe chip. Unfortunately, the length of the curing process (4-8 hours per layer) and affinity between silicon and PDMS caused the liquid coating to creep up into the comb-drive and permanently damage the probe. The final solution was to use an UV-cured adhesive (NOA-60, Norland Products Inc.) in place of PDMS. A small polymer sphere was created at the probe tip by applying multiple layers of NOA-60. Each layer took around one minute to cure under a 380nm UV-lamp. To protect the rest of the probe from the UV light, a sheet of aluminum foil was wrapped around the probe chip. The treated probe could stably provide sufficient adhesion for a droplet of up to 8µL in volume while being much less prone to failure. Figure 2.5 shows a photo of an NOA-60 dip-coated probe.

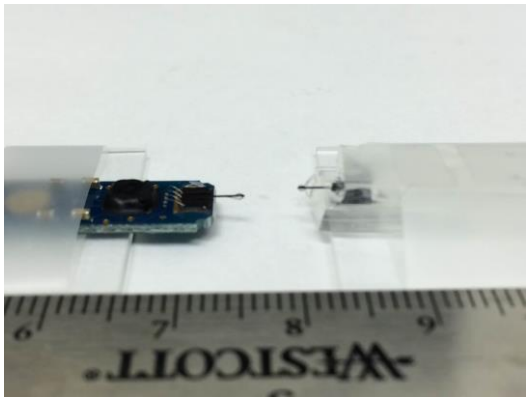

Figure 2.5: NOA coated probe shown with a ruler. Right: a dummy probe made of PDMS used for testing the procedure.

2.1.3 Sample Preparation

A portion of the PDMS samples used in the experiments was made earlier by Huan Li[12], while newer samples were designed and made by Xian Wei[19]. Molds of the PDMS samples were manufacture using SU-8 2015 (MicroChem Inc.). SU-8 was first spin-coated to a 4-inch silicon wafer. The wafer was then softbaked and exposed using a high-resolution chrome mask. After postbaking, development and hardbaking, a non-sticking layer of silane was applied to the mold to complete the procedure. More details on the manufacturing of the molds can be found in Li[12].

Several parameters were of particular interest to the study. These include shape of pillar top (circular/square), alignment of the pillars (rectangle/square/hexagonal lattice), characteristic size of the pillar (diameter/side length) and the area fraction, α, defined as the ratio of pillar top area to total projected area of a unit cell (see section 1.3). Table 2.1 shows a list of samples used in the experiments including theoretical contact angles with water. The contact angles were calculated using the Cassie-Baxter model, with a homogeneous PDMS-water contact angle of 114^{o} determined using a goniometer.

Table 2.1: PDMS samples used in experiments

Sample Number	Pillar Specs				Area Fraction (α)	Contact Angle (Theoretical) (degrees)
	Arrangement	Shape	Size (μm)	Spacing (μm)		
1	Square	Circular	45.7	112.3	0.13	157.4
2	Square	Circular	47.7	81.3	0.27	147.1
3	Square	Circular	54.7	83.1	0.34	143.0
4	Square	Circular	45.2	57.2	0.49	135.2
5	Square	Circular	32.1	69.0	0.17	154.0
6	Square	Circular	36.5	64.7	0.25	148.4
7	Parallel	1D Ridge	30.2	78.5	0.38	140.8

2.1.4 Synchronization

Since image capturing and stage motion were controlled by separate programs, synchronization of the video and force signal was required. In experiments this was done by causing a small displacement of the optical table. The ensuing vibration could then be captured by both the camera and the force probe. The damping system on the table ensured that the vibration died off before stage movement and data collection started.

2.2 Results and Discussion

2.2.1 Environmental Noise

Figure 2.6 shows a sample of background noise taken with the full experimental setup. The average magnitude of noise was found to be around 1 μN, which could severely hinder interpretation of the force signal, as the smaller saw-tooth features ranged from 5 to 8 μN. Therefore specific effort was made to identify the sources of noise signals and eliminate them from the force measurements. The Fourier spectrum of the signal is shown in Figure 2.7a, where three peaks are found at 250, 260 and 270 Hz. By comparison, the corresponding peaks were strongly suppressed in a later measurement (Figure 2.7b). As it turned out, the ventilation system used in the lab was shut off during

the second measurement which caused a reduction of noise strength in the 250-300 Hz range. A third noise measurement, shown in Figure 2.8, revealed another source of noise. The camera system used for motion capture contained a high power cooling fan whose exhaust introduced a significant overall increase of noise strength. This was not noticed earlier, as the air flow pattern varied depending on positioning of the experimental apparatus. To eliminate this particular noise signal, a simple cupboard shielding was used to isolate the sample and probe from the fan exhaust (Figure 2.9).

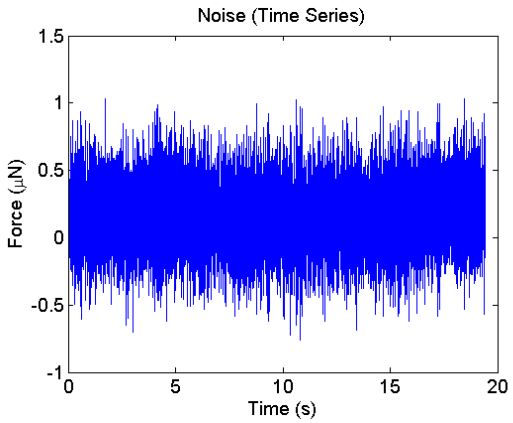

Figure 2.6: A sample of noise signal. The probe was not in contact with the droplet for the duration of this recording.

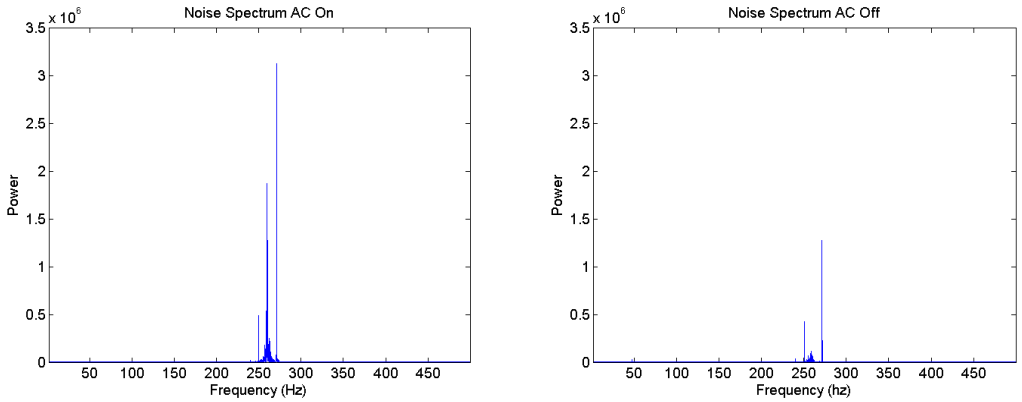

Figure 2.7: Frequency spectra of noise measurements conducted with the AC system on (left) and off (right). In both plots three peaks can be seen at 250, 260 and 270 Hz. However, the noise strength is considerably weakened with the AC shut down (more than halved in power).

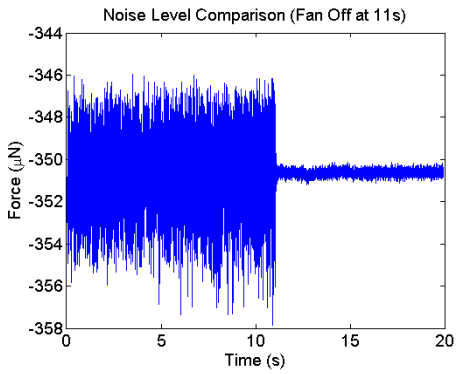

Figure 2.8: Noise measurement showing effects of the cooling fan. The fan was shut down at 11s mark and caused a significant reduction in noise level. Considering that the effects of the fan exhaust depended on the setup of apparatus and thus did not have a unique frequency range, shields were used over a frequency filter.

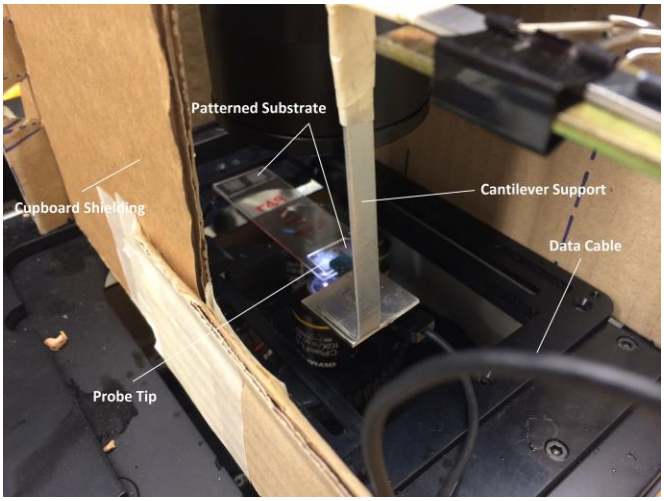

Figure 2.9: photo showing the cupboard shielding used to eliminate effects from fan exhaust.

Figure 2.10a shows a section of actual force data after eliminating the environmental noises. The frequency spectrum is shown in Figure 2.10b. The main periodicity of the triangular behavior resulted from the depinning of pillar columns perpendicular to substrate movement. In this case, the substrate speed was 160 μm/s and column to column spacing in the pillar array was 83 μm, giving a main period of 0.5 seconds. A higher frequency oscillation was also observed around 30Hz, corresponding to the smaller periodic features inside each main period. When attempting to remove the 30Hz peak, it was found that the free response of the droplet at the beginning of the recording also disappeared (Figure 2.10c).

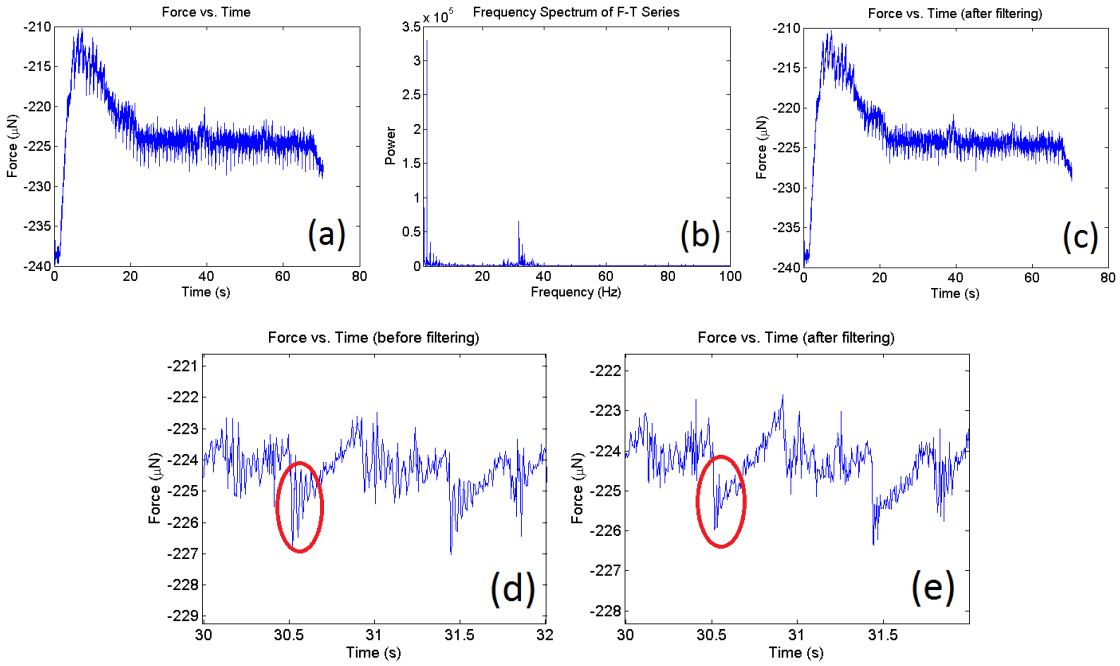

Figure 2.10: (a) original force-time series. (b) Frequency spectrum of the original data. (c) Force-time series after 30Hz peak was filtered. (d)(e) Enlarged view of plot (a) and (c). Sample 5 was used. By comparison between (d) and (e), the 30Hz peak is most easily identified as the "aftershock" at the end of each saw-tooth feature (red circles in (d) and (e)). A possible explanation is that the sudden movement of the droplet at the depinning of the receding contact line excited the cantilever-droplet system, while the oscillation is dampened during the subsequent deformation of the droplet before the next depinning event occurs.

The initial vibration was designed to synchronize the video and force signal and was introduced by a kick to the optical table. Since stage motion started after the initial vibration died off, it followed that the same frequency observed inside the main periodicity must be the natural oscillation of either the droplet or the cantilever beam supporting the probe (see Figure 2.2b) excited by substrate movement. A detailed analysis for the oscillation frequency associated with a droplet with pinned contact line can be found in section 2.2.3. As for the natural frequency of the cantilever beam, a separate noise measurement without contact with a liquid droplet was conducted. The initial displacement was introduced similarly and the free response of the cantilever-probe structure was recorded. Figure 2.11a shows the force-time plot of the noise recording. A kick was applied at t=1.88 second. Two power spectra, Figure 2.11b and 2.11c, were constructed for the signal before and after the free response started. A distinct

peak appeared after the kick at 24.6 Hz. Even though the measured frequency was slightly lower than the observed noise peak, it is believed that the oscillation of the cantilever beam was the source of the noise, since the supporting structure had to be assembled manually before each experiment and thus variation in its natural frequency is expected.

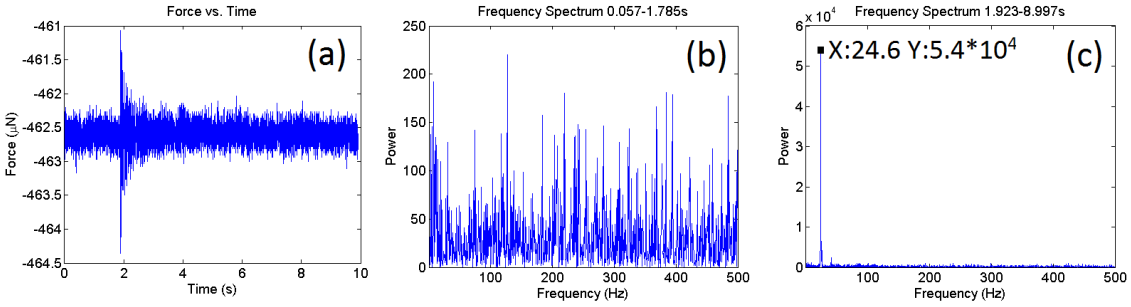

Figure 2.11: (a) noise signal containing the kick (1.88s). (b) Spectrum of the noise signal before 1.88s. (c) Spectrum of the noise signal after 1.88s. A single peak at 24.6 Hz emerged as the system was excited by the kick. Since the probe was not attached to any droplet, the above measurement confirmed the cantilever beam as the source of the oscillation near 30 Hz.

2.2.2 Free Oscillation of Droplet

Attempts were made to identify the mode of oscillation observed as a potential source for a higher frequency observed in the force signal. For oscillations governed by surface tension restoring forces, the oscillation frequency of order (meridional) l and degree (azimuthal) m takes the form:

$$\Omega_{ml} = \sqrt{\frac{\gamma_{lg}}{\rho_l V \lambda_{ml}}} \tag{2.1}$$

Here λ_{ml} is the eigenvalue of an oscillation mode of order l and degree m. For a free droplet oscillating about a spherical shape, Lamb[20] proposed the following formula for eigenvalues:

$$\lambda_{ml} = \frac{3(m+1)}{4\pi m(m^2-1)(m+2)} \tag{2.2}$$

The $m = 0$ mode is forbidden as a free surface mode because it requires volume change of incompressible liquid. The $m = 1$ mode is also forbidden since it amounts to

translation of the entire droplet with no deformation, and therefore no restoring forces. However, for a droplet pinning on a rigid surface, the $m = 1$ mode becomes possible, as illustrated in Figure 2.12.

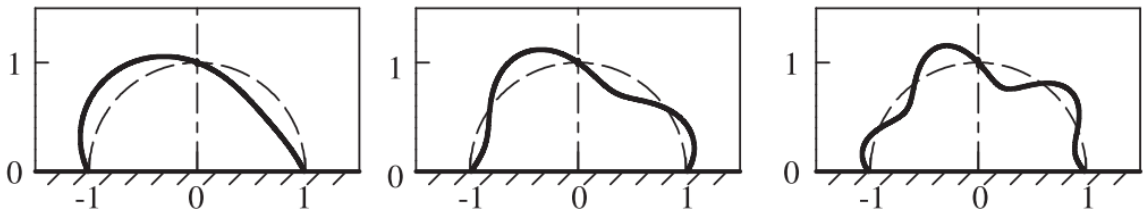

Figure 2.12: Degree 1 surface modes of a pinned droplet. From left to right: l=1, l=2, l=3. Profiles were taken from Chiba et al.[23]

Lyubimov[21] established a dispersion relation for this mode of oscillation:

$$\omega^2 S(\omega) = -\frac{2}{1+\rho^*} \tag{2.3}$$

$$S(\omega) = \omega^2 \sum_{n=1,n\ odd}^{\infty} \frac{F_n P_n^{(1)}(0)}{\Omega_n^2 - \omega^2} - \frac{1}{3} \tag{2.4}$$

Here ρ^* is the dimensionless density of the liquid (defined in Equation 2.6), Ω_n are the fundamental oscillation frequencies of a free spherical droplet (Ω_{nl} following the notation of equation 2.1, but by equation 2.2 the non-axisymmetric modes ($l \neq 0$) are degenerate), P_n are the n-th order Legendre polynomial, and F_n are coefficients defined as:

$$F_n = -\frac{2}{3}\frac{(2n+1)P_{n-1}(0)}{(n^2-1)(n+2)} \ \ (n \neq 1), \ \ F_1 = \frac{2}{3}\ln 2 - \frac{11}{18} \tag{2.5}$$

The non-dimensional parameters for frequency and density are:

$$\Omega = \sqrt{\frac{\gamma_{lg}}{(\rho_l+\rho_g)R^3}}, \ \ \rho = \rho_l + \rho_g \tag{2.6}$$

Assuming negligible gravitational effects, the droplet will assume a spherical cap shape, the radius of which can be calculated from geometry:

$$R = \left(\frac{3V}{\pi(\cos^3\theta - 3\cos\theta + 2)}\right)^{\frac{1}{3}} \tag{2.7}$$

Solved numerically, the lowest frequency occurred with meridional mode number 1 ($l = 1$, determined by magnitudes of the roots) with a dimensionless value of 2.2198 (ω=342.26 rad/s, 54.47 Hz). Albeit higher than the observed oscillation frequency, the 1-1 mode was the slowest possible oscillation a pinned droplet could attain. Discrepancies between the model assumption and the experimental condition did exist: Lyubimov assumed a 90-degree contact angle and no external effects, while in our experiment the stationary contact angle was 114 degrees for smooth surfaces and higher for patterned surfaces depending on the area fraction α. Additionally, the droplet was subject to external constraints from the contact with the force probe. Further work is required to understand the effects from the extra conditions and to determine the oscillation frequency of a constrained droplet.

2.2.3 Residual Liquid

As the droplet moves on the substrate, the receding contact line undergoes periodic pinning and depinning. A more careful look at the captured videos revealed that tiny bits of liquid were left on pillars from which the contact line de-pinned (see Figure 2.13). The observation was largely neglected in earlier experiments in this study since the size of the residual is limited by pillar size and therefore the fluorescence signal from the residual drops is overwhelmed by that of the highly luminous bulk liquid. Evaporation of the liquid also resulted in a very short time window within which the light emission from the residual liquid could be captured. However, using a less volatile water-glycerol mixture and enhanced exposure focused at the trailing edge of the droplet, the residual droplets could be clearly resolved. To better understand the formation of tiny droplets, experiments were conducted on substrates with grooved patterns (sample 7, see Figure 2.14) with very low movement speed (8μm/s). It was found that prior to contact line depinning, a bridge formed between the bulk liquid and the pillar. The bridge then underwent elongation and radial contraction before breaking off. Figure 2.13 shows a series of screenshots during the formation and breakage of the liquid bridge. This observation raised interesting questions to the study: on what spatial and temporal scale does the liquid bridge affect the morphology of the droplet? How does the said effect manifest in the force measurement? Lastly, does the absence of liquid bridges in the

simulation invalidate the computational model or imply insignificance of bridge formation and breakage?

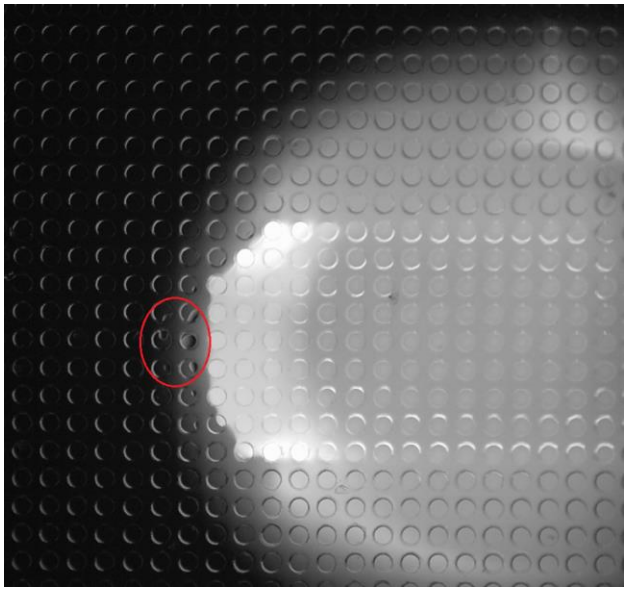

Figure 2.13: Screenshot showing residual liquid behind the trailing edge. Droplet volume was 6uL and substrate speed was 80um/s. Water was used as the testing liquid, resulting in fast evaporation of the residual liquid. Sample (4) was used (See Table 2.1).

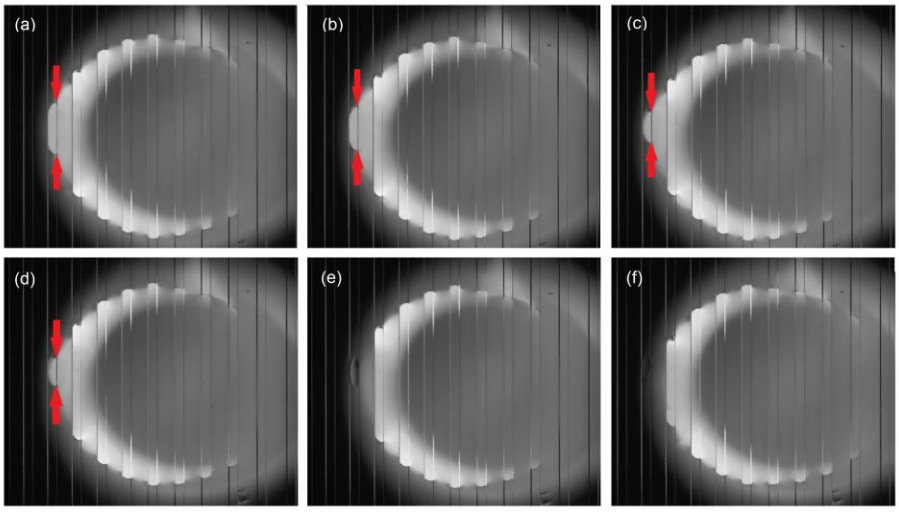

Figure 2.14: screenshots showing the formation and pinching of a liquid bridge on a grooved pattern (sample 7, groove spacing 78.5μm, α=0.38). The red arrows mark the location of the liquid bridge. Breakage occurred in (e). a) Starting configuration. b) The trailing ridge started to dewet. c) A neck formed between the build liquid and pinned drop. d) The neck continued to develop. e) A small drop broke off the build liquid. f) Evaporation of the residual droplet.

Various studies have looked into liquid deposition at the trailing edge of a droplet on patterned surface. Using a non-volatile variant of the UV-cured adhesive NOA (NOA72, Norland Products Inc.), Dufour et al characterized the volume distribution of liquid deposits following the receding contact line of a droplet[4]. Wang et al[5] discussed two modes of liquid bridge failure, tensile (normal to the surface) and sessile (parallel to the surface) and offered a qualitative explanation of the process. In a more fundamental study of liquid pinching and droplet formation, Eggers et al studied a one-dimensional axisymmetric column of liquid with gravity acting axially (z-direction). The following equations of motion were proposed[22]:

$$\partial_t v = -vv_z - \frac{p_z}{\rho_l} + \frac{3\nu(h^2 v_z)_z}{h^2} - g \tag{2.8}$$

$$p = \gamma_{lg}\left[\frac{1}{h(1+h_z^2)^{\frac{1}{2}}} - \frac{h_{zz}}{(1+h_z^2)^{\frac{3}{2}}}\right] \tag{2.9}$$

$$\partial_t h = -vh_z - \frac{1}{2}v_z h \tag{2.10}$$

Here v is the fluid velocity, p is the pressure due to surface tension, and h is the radius of the liquid column. z is the coordinate along the axial direction and the subscript z refers to derivative with respect to z. The boundary conditions for a solution in $z \in [-l, l]$ are:

$$h(\pm l, t) = h_{\pm} \tag{2.11}$$

$$v(\pm l, t) = v_{\pm} \tag{2.12}$$

In reality, the bridge formed between the droplet and the residual liquid intersects with the substrate at various angles depending on the location of the pinning pillar. Nevertheless, since the Bond number, $Bo = \frac{\rho_l g L^2}{\gamma_{lg}}$, is small for typical liquid bridge dimensions (for L=70μm and water, Bo=6.57x10^{-4}), we expect minimal discrepancy from orientation of the liquid column. Figure 2.15 shows a plot from [22] of the solution to the above set of equations.

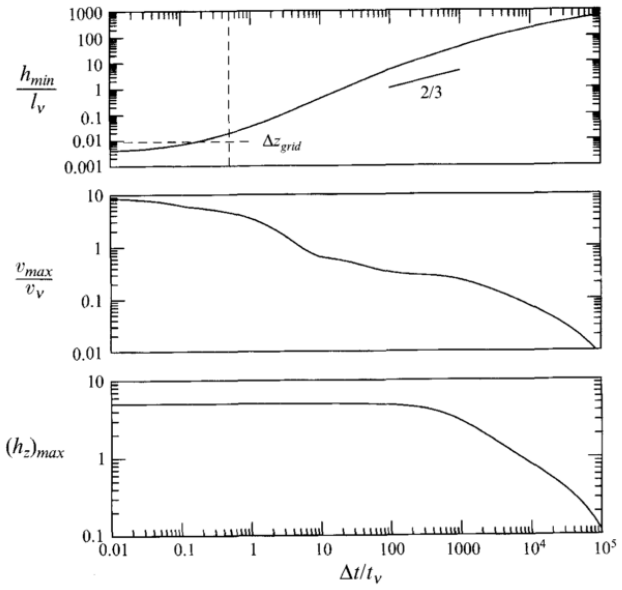

Figure 2.15: Plots summarizing the numerical solution of Eggers et al[22]. From top to bottom: minimum radius of the liquid bridge, maximum axial velocity of fluid, maximum derivative of bridge radius. Δt represents time prior to singularity. A viscous length and time scale was used as discussed in 2.2.3. By providing a starting column radius, an estimation of column collapse time can be obtained using the 2/3 slope illustrated and the resolution limit marked by the crossing of the dashed lines in the first plot.

The non-dimensionalizing parameters for length and time were:

$$l_\nu = \frac{\rho_l \nu^2}{\gamma_{lg}},\ t_\nu = \frac{\nu^3 \rho_l^2}{\gamma_{lg}^2} \tag{2.13}$$

For water at 20°C, the viscous length and time scales were respectively $1.38\text{x}10^{-8}$m and $1.91\text{x}10^{-10}$s. Using the $\frac{2}{3}$-slope that underlined the radius-time plot, an overestimate of the collapse time of a water column with starting radius 20 μm was found to be $1.05\text{x}10^{-5}$s. Under the same condition, a liquid column of 1:1 water-glycerol (properties taken with volumetric average) mixture would collapse in $1.15\text{x}10^{-5}$s. Typical sampling rate of the force data ranged from 200Hz to 1000Hz. Therefore neither of the time scales was large enough to be resolved by the force probe. Admittedly, in an actual experiment there was no clearly defined boundary of the liquid bridge or a time stamp marking the start of collapse. Nevertheless, on the order of one-hundredth of the minimum sampling interval, effects from the formation and pinching of liquid bridges could not be registered in the

experimental measurements and thus could be safely neglected in interpreting the force data.

2.2.4 Force Measurements

The focus of the experimental effort was the attempt to explain behavior of the force-displacement curve in terms of geometric features of the deformed droplet due to relative motion with respect to the substrate. In some earlier work[12] Huan Li established a correlation between the maximum and steady state force, denoted F_m and F_s, and the area fraction of the substrate, α. Figure 2.16 shows an illustration of the force definitions. Figure 2.17 shows a plot from [12] summarizing the observed correlation between area fraction α and the forces F_m and F_s. Resistance to motion originates from segments of contact line pinned to individual pillars; therefore a greater area fraction would provide more pinning sites for the same droplet volume. In terms of the force definitions, both F_m and F_s increase with area fraction. However, additional work was required concerning more detailed features, including the triangular wave pattern during the steady state of motion and other sub-period patterns.

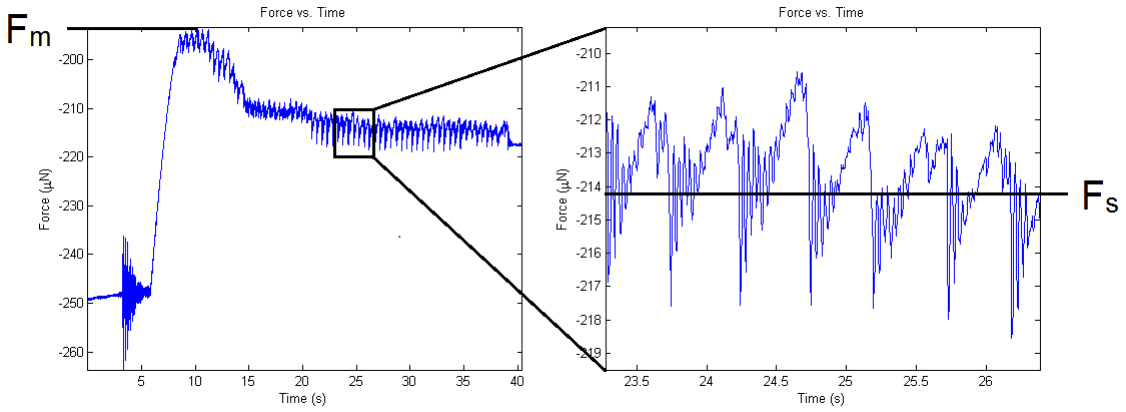

Figure 2.16: definition of the maximum force, F_m, and the steady-state force, F_s.

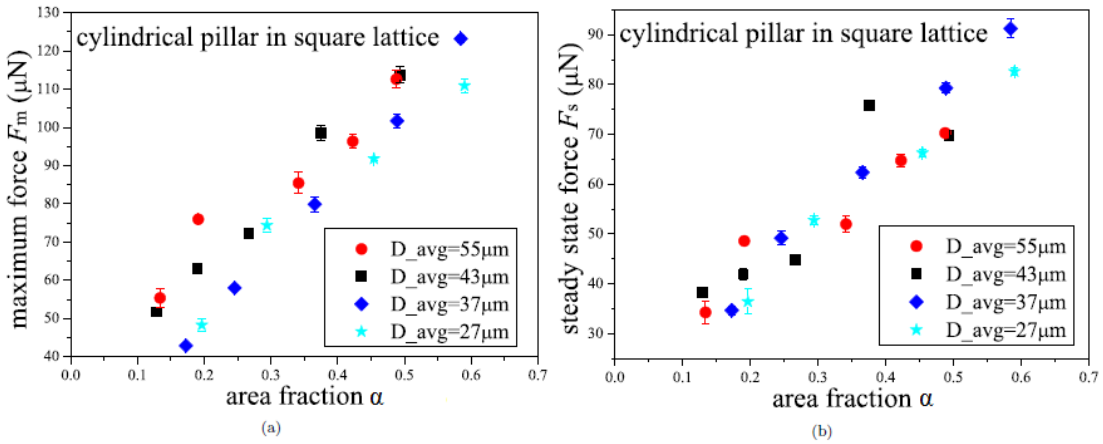

Figure 2.17: plots showing changes of F_m and F_s with area fraction[12]. D_avg denotes the averaged pillar diameter. The original plots used φ as symbol for area fraction. The axis labels were changed to α in accordance to notation used in this article.

One of the improvements made in the present study was the employment of a band-pass filter that only removes higher frequency features upon identifying the source of the feature. In the original analysis, the force data underwent a 10-20 sample smoothing function which indiscriminately removed all higher frequency features. This introduced additional difficulties in distinguishing noise signals from geometry-based force responses. The improved procedure addresses the issue by abandoning the smoothing function and focusing on the frequency spectrum. Figure 2.18 showed a processed force-displacement curve with all previously identified noise signals filtered. Initially the liquid droplet underwent elongation due to movement of the force probe. During this process the receding contact line remained pinned and the overall resistance increased. The deformation continued until a maximum force F_m was achieved, upon which depinning started along the trailing edge. The ensuing depinning events further decreased overall resistance and the shape of the contact area stabilized toward an elongated ellipse with straight side edges. Finally, the steady state was characterized by a constant average resistance F_s and small saw tooth features corresponding to the depinning of entire columns of pillars perpendicular to the direction of movement at the receding contact line. As was discussed in the simulation section, the positive slope in the increasing portion of the saw tooth resulted from the elastic response of the droplet surface to deformation.

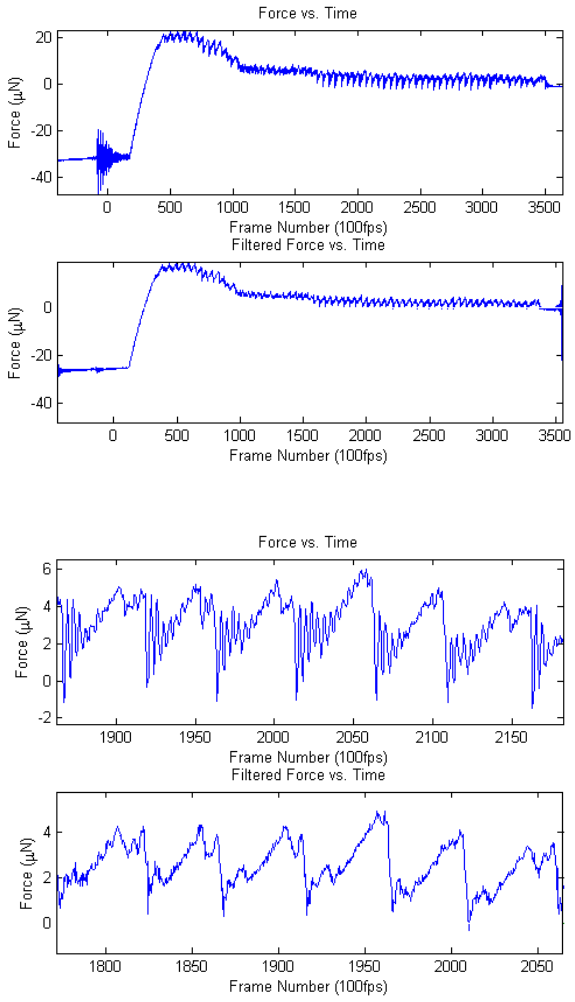

Figure 2.18: Original and filtered force data (6ul water-glycerol mixture, 160um/s, sample (5)).

It was still unclear whether individual pinning and depinning events were responsible for the more irregular features inside each period. As this article was written there were still ongoing effort trying to identify effects of the individual events in the force-displacement data.

2.3 Conclusion

Liquid droplets moving on a patterned substrate were studied using a procedure developed in Li[12]. Dynamic resistance force data was collected by a capacitor probe and visual information was obtained by a high speed camera. Features in the force-displacement curve were studied in the frequency domain and possible noise sources including environmental air flow and surface modes of the pinned droplet were discussed.

Residual droplets formed by liquid bridge pinching were found using low volatility water-glycerol mixture as test liquid. Literature review eliminated the formation and breaking of liquid bridges as features manifested in the force-displacement data, as the time interval required for these processes was on the order of one-hundredth of the minimum sampling interval. Lastly, the positive slopes measured from the periodic saw teeth features confirmed the elastic response observed in the dynamic simulations.

Additional work will be required to explain the large discrepancy between theoretically predicted surface mode frequencies and observed droplet oscillation. In addition, individual pinning and depinning events were possible factors that could leave a footprint in the force-displacement data and further examination is required.

References

1. Blossey, R. Self-Cleaning Surfaces – Virtual Realities. *Nature Materials* **2**, 301-306 (2003)

2. Burton, Z. & Bhushan, B. Surface Characterization and Adhesion and Friction Properties of Hydrophobic Leaf Surfaces. *Ultramicroscopy* **8-9**, 709-719 (2006)

3. Krumpfer, J., Bian, P., Zheng, P., Gao, L. & McCarthy, T.J. Contact Angle Hysteresis on Superhydrophobic Surfaces: An Ionic Liquid Probe Fluid Offers Mechanistic Insight. *Langmuir* **27**, 2166-2169 (2011).

4. Dufour, R., Brunet, P., Harnois, M., Boukherroub, R., Thomy, V. & Senez, V. Zipping Effect on Omniphobic Surfaces for Controlled Deposition of Minute Amounts of Fluid or Colloids. *Small* **8**, 1229-1236 (2012)

5. Wang, Y. & McCarthy, T. J. Dip-Coating Deposition on Chemically Patterned Surfaces: A Mechanistic Analysis and Comparison with Topographically Patterned Surfaces. *Langmuir* **30**, 2419-2428 (2014)

6. Cassie, A.B.D. & Baxter, S. Wettability of Porous Surfaces. *Trans. Faraday Soc.* **40**, 546-551 (1944)

7. Hao, P., Lv, C., Yao, Z. & He, F. Sliding behavior of water droplet on superhydrophobic surface. *EPL (Europhysics Lett)* **90,** 66003 (2010).

8. Mahadevan, L. & Pomeau, Y. Rolling Droplets. *Phys Fluids* **11,** 2449–2453 (1999).

9. Quere, D. Drops at Rest on a Tilted Plane. *Langmuir* **14,** 2213–2216 (1998).

10. He, B., Lee, J. & Patankar, N.A. Contact Angle Hysteresis on Rough Hydrophobic Surfaces. *Colloids and surfaces A* (**1-3**), 101-104 (2004).

11. Kulinish, S.A. & Farzaneh, M. Effect of Contact Angle Hysteresis on Water Droplet Evaporation from Super-Hydrophobic Surfaces. *Applied surface science* **8**, 4056-4060 (2009).

12. Li, H. Solid-Liquid Interactions in Microscale Structures and Devices. 1–137 (2011).

13. Brakke, K. Surface Evovler Documentation. (2013).

14. Jansen, H.P., Bliznyuk, O., Kooij, E.S., Poelsema, B. & Zandvliet, H.J.W. Simulation Anisotropic Droplet Shpaes on Chemically Striped Patterned Surfaces. *Langmuir* **28**, 499-505 (2012).

15. Martino, P., Freeman, G., Racz, L. & Szekely, J. Predicting Solder Joint Shape by Computer Modeling. In Proceedings of the 44th Electronic Components and Technology Conference,Washington, DC, (1994).

16. Harsh, K. F., Bright, V. M. & Lee, Y. C. Solder Self-Assembly for Three-Dimensional Microelectromechanical Systems. *Sensors Actuators A Phys* **77,** 237–244 (1999).

17. Dorrer, C. & Rühe, J. Contact Line Shape on Ultraphydrophobic Post Surfaces. *Langmuir* **23**, 3179-3183 (2007).

18. Grigola, M. Effects of Micro- And Nano-Scale Surface Geometry on Behavior of Live Cells And Liquid Deoplets. 1-128(2013).

19. Wei, X. Stick-Slip Behavior of Liquid Droplets on Pillar-Arrayed PDMS Surfaces. (2014).

20. Lamb, H. On the Oscillations of a Viscous Spheroid. *Proc Lond Math Soc.***1**. 51-70 (1881).

21. Lyubimov, D., Lyubimova, T. & Shklyaev, S. Non-Axisymmetric Oscillations of a Hemispherical Drop. *Fluid Dynamics* **6**. 851-862 (2004).

22.Eggers, J. & Dupont, T. Drop Formation in a One-Dimensional Approximation of the Navier-Stokes Equation. *J. Fluid Mech.* 205-221 (1994).

23. Chiba, M., Michiue, S. & Katayama, I. Free Bivration of a Spherical Liquid Drop Attached to a Conical Base in Zero Gravity. *Journal of Sound and Vibration* **331**. 1908-1925 (2012).

24. Meseguer, J. The Breaking of Axisymmetric slender Liquid Bridges. *J. Flguid Mech*. 123-151 (1983).

25. Eggers, J. Universal Pinching of 3D Axisymmetric Free-Surface Flow. *Physical Review Letters* **21**. 3458-3460 (1993).

26. Brenner, M., Shi, X. & Nagel, S. Iterated Instabilities during Droplet Fission. *Physical Review Letters* **25**. 3391-3394 (1994).

27. Shi, X., Brenner, M. & Nagel, S. A Cascade of Structure in a Drop Falling from a Faucet. *Science* **5169**. 219-222 (1994).

28. Brenner, M., Lister, J. & Stone, H. Pinching threads, singularities and the number 0.0305… *Physics of Fluids*. 2827-2836 (1996).

29. Eggers, J. Nonlinear Dynamics and Breakup of Free-Surface Flows. *Reviews of Modern Physics* **3**. 865-930 (1997).

30. Chen, W., Fadeev, A. & Hsieh, M. Ultrahydrophobic and ultralyophobic surfaces: some comments and examples. *Langmuir* **13**. 3395-3399 (1999).

31. Cohen, I., Brenner, M., Eggers, J. & Nagel, S. Two Fluid Drop Snap-Off Problem: Experiments and Theory. *Physical Review Letters* **6**. 1147-1150 (1999).

32. Patankar, N. & Chen, Y. Numerical simulation of droplet shapes on rough surfaces. *Nanotech* **2**. 116-119 (2002).

33. Tadmor, R. Line energy and the relation between advancing, receding and young contact angles. *Langmuir* **18**. 7659-7664 (2004).

34. Anantharaju, N., Panchagnula, M., Vedantam, S., Neti, S. & Tatic-Lucic, S. Effect of three-phase contact line topology on dynamic contact angles on heterogeneous surfaces. *Langmuir* **23**. 11673-11676 (2007).

35. Gao, T. & McCarthy, T. How Wenzel and cassie were wrong. *Langmuir* **7**. 3762-3765 (2007).

36. McHale, G. Cassie and Wenzel: were they really so wrong? *Langmuir* **15**. 8200-8205 (2007).

37. Semprebon, C., Mistura, G., Orlandini, E., Bissacco, G., Segato, A. & Yeomans, J. Anisotropy of water droplets on single rectangular posts. *Langmuir* **10**. 5619-5625 (2009).

38. Xiao, R., Enright, R. & Wang, E. Prediction and optimization of liquid propagation in micropillar arrays. *Langmuir* **19**. 15070-15075 (2010).

39. Ng, T. & Panduputra, Y. Dynamical force and imaging characterization of superhydrophobic surfaces. *Langmuir* **1**. 453-458 (2012).

40. Raj, R., Enright, R., Zhu, Y., Adera, S and Wang, E. Unified model for contact angle hysteresis on heterogeneous superhydrophobic surfaces. *Langmuir* **45**. 15777-15788 (2012).

41. Paxson, A & Varanasi, K. Self-similarity of contact line depinning from textured surfaces. *Nature communications*. 1492 (2013).

42. Milne, A., Defez, B., Cabrerizo-vilchez, M. & Amirfazli, A. Understanding (sessile/constrained) bubble and drop oscillations. *Advances in Colloid and Interface Science* **203**. 22-36 (2014).